

High-quality surface microseismic data illuminates fracture treatments: A case study in the Montney

BRADLEY BIRKEL, KONRAD CIESLIK, BEN WITTEN, SUMMER MONTGOMERY, and BRAD ARTMAN, Spectraseis
DAVID MILLER and MARK NORTON, Progress Energy Resources

Monitoring hydraulic fracture stimulations from the surface is a technique that, in the past, met with mixed success. One reason for this experience is that the measurement has often been treated as if it were only a minor variant of the reflection surveys our industry is most familiar with. While reflection seismic sources are designed to generate primarily P-waves, fracturing rocks emit both P- and S-waves with the much larger proportion of energy as S-waves. To capture the information content in the microseismic wavefield, surveys must be designed to record, and processing strategies designed to use, the full vector wavefield energy emitted by the fracture process. To record the full vector wavefield requires the use of appropriate sensors capable of recording low frequencies and three components.

Vertical borehole arrays remain the staple of the microseismic industry because they put recording equipment near the target and produce a volume of data easily handled by data processors. Surface recording, however, offers distinct advantages over the borehole. Primary among them is that no borehole is needed, which can radically reduce costs. Secondly, a surface array provides increased and uniform accuracy of the lateral location of events without measurement bias, regardless of where the event originated along the length of the lateral. Thirdly, a large surface array will capture enough of the radiation pattern of the microseismic events to allow reconstruction of the fracture mechanism.

In this paper, we show how to get the most information out of a surface array using a case study from the Montney Formation. This program produced high-quality microseismic data and demonstrates the extent of what is possible with surface recording. We will discuss which observations are expected to be universal, and which are likely locally controlled.

Of critical importance to the success of this project were the survey geometry, the use of three-component (3C) broadband seismic sensors, good velocity control, and both acoustic and elastic processing capabilities. We will discuss the value of both the P- and S-waves in our experience, and show the dominant failure mechanism associated with two distinct fracture patterns uncovered in the data. Combining these observations and techniques, we demonstrate how surface microseismic data is used for determining which portions of the reservoir have been stimulated and potentially propped. This mapping can serve as input to decisions on well spacing, perf spacing, and reserve calculations for the geoscientists and engineers working on these wells.

Seismic emissions from fracturing

Perhaps the oldest field of geophysics is earthquake monitoring and mapping. From this field came hypocenter mapping and source mechanism characterization, which are the basis

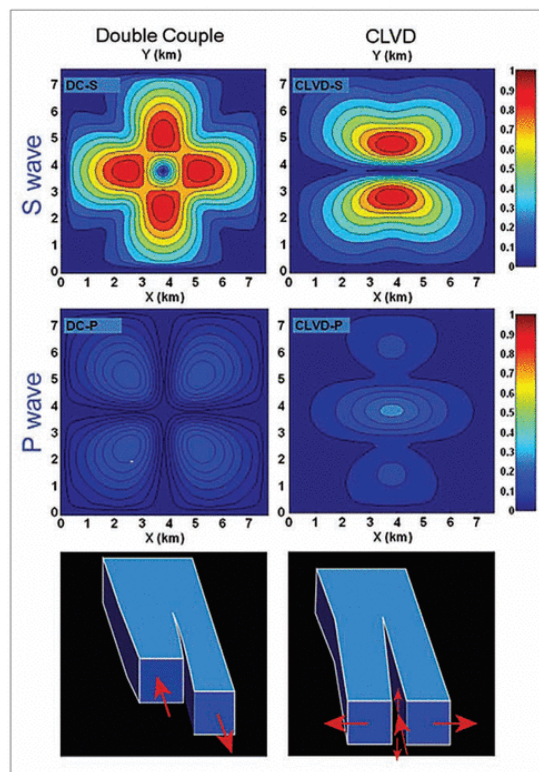


Figure 1. Surface energy distribution from modeled double couple and CLVD fractures.

for the petroleum industry's emergent microseismic technology. Fractures seen in petroleum microseismic data can be mathematically decomposed into percentages of three end-member fracture types: isotropic, compensated linear vector dipole (CLVD), and double couple (DC). A description of how this can be done is found in Baig and Urbanic (2008). Each fracture type describes the different particle motion of the fracturing rock as well as the directional radiation pattern of the different P- and S-wave energy generated by the fracture. Modeling the energy radiation patterns produced when a fracture is created is an important first step in designing a proper receiver array to capture this information.

Figure 1 shows the P- and S-wave energy arriving at the Earth's surface from modeled vertical DC and CLVD sources. The radiation patterns and amplitude calculations for DC are found in Aki and Richards (2002), while the similar CLVD relationships are in Lokmer and Bean (2010). The V_p/V_s ratio used was 2.0.

PASSIVE SEISMIC AND MICROSEISMIC—PART 1

In the case of the DC event, P-wave energy arrives in a four-leaf-clover pattern with the main energy located at 45° to the fracture plane. S-wave energy from the same fracture arrives in a similar four-leaf-clover shape, rotated 45° from the P-wave maxima. The most important contrast between the P- and S-wave energy is that the DC failure mechanism initiates 16 times more energy as S-waves than P-waves. Note that the only spot in the array that receives no P- or S-wave energy from the DC event is directly over the fracture event. The CLVD source produces a maximum of P-wave energy over the fracture location and two flanking S-wave lobes. The orientation of the fracture plane is defined by the zero-amplitude node between the two S-wave lobes. The energy of the S-wave for this fracture type is stronger than the P-wave by a factor of 12.

The distribution of energy in such patterns is diagnostic of the rock failure, whether a tensile opening or shearing fracture. However, it is possible to make these inferences only with data from a surface array, or at least two borehole arrays with sufficient sampling to capture the characteristic energy radiation of the different fracture types.

Reflection seismic surveys, with relatively rare exceptions, use a source designed to produce primarily P-waves and recording equipment designed and optimized for recording only the P-wavefield. Microseismic wavefields are fundamentally different geophysical data. As such, fit-for-purpose hardware and processing algorithms greatly minimize the risk of disappointing survey results. On the hardware side, this means using 3C instruments with low-corner frequencies of 5 Hz or less. Once collected, the dominant S-wave energy should be an integral part in the processing (Witten et al., 2012) as they help in characterizing the radiation pattern.

Montney case history

Project description. The Montney Shale of northeast British Columbia is one of Canada's most important developing unconventional reservoirs. It was deposited in a foreland basin during the Triassic, with thickness in excess of 300 m. In some places, the Montney is thick enough for operators to develop

the formation at multiple stratigraphic levels. The shale trend produces both dry gas and liquids, depending upon the area. The geology can be complex, requiring that operators study not only the mineralogical changes in the formation, but also the structural overprint of the Rocky Mountain foothills.

Figure 2 shows the project location and a diagram of the two treatment wells, with the recording grid deployed at the surface for microseismic monitoring. No boreholes were available at this location for deploying a downhole array. Two intervals were stimulated in a zipper-frac configuration, with successive frac stages alternating between two wellbores in the Upper Montney (2000 m TVD) and Lower Montney (2200 m TVD).

3D seismic data had recently been acquired in the area, from which time horizons were extracted. Dipole sonic-log data were used to construct the P- and S-wave velocity models shown in Figure 2 by extrapolating the well-log-measured velocities, guided by the seismic horizons. Important to the project's success was the coverage of the dipole sonic log that was run from the reservoir to the base of the surface casing, providing excellent constraints to the local P- and S-velocities along virtually the entire travel path of the microseismic energy.

Acquisition. The acquisition program for this project used 200 high-sensitivity (1500 V/m/s), 3C broadband (0.025–100 Hz) sensors deployed over the treatment wells with 250-m station spacing in a regular grid totaling 11 km². The survey area is heavily forested with topographic relief of several hundred meters. The grid was oriented to facilitate access to the station locations. The acquisition system was entirely nodal, with one 3C sensor and digitizing recorder per station. This made the design and layout of the grid highly efficient with no new-cut lines required. The array was deployed in six days by a small, ten-person crew with no lost-time HSE incidents. The array recorded continuously for the nine days of the fracture treatments without any downtime.

Data processing. There are two main workflow stages for processing microseismic data: detection and analysis. The detection stage involves independent partial migrations of the

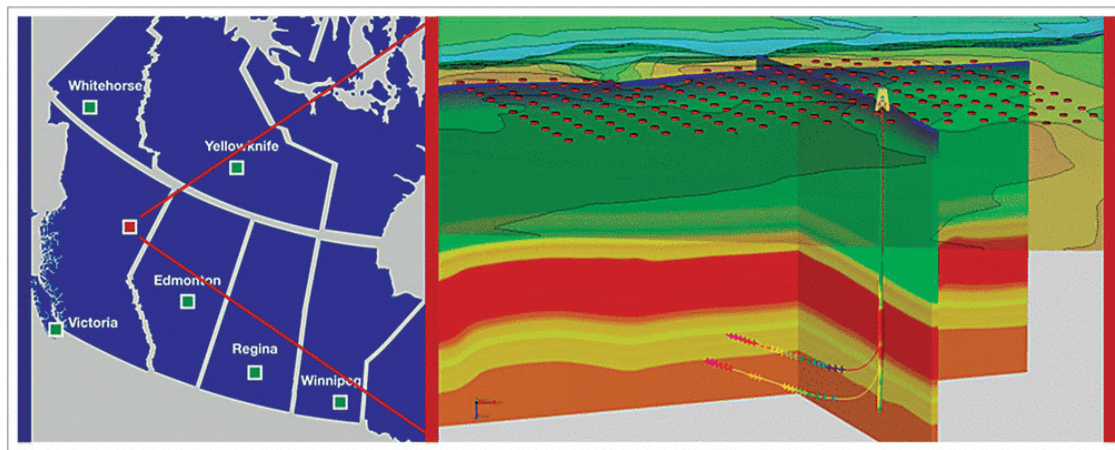


Figure 2. Project location map with a detailed view of the surface microseismic grid and the stimulated wells.

PASSIVE SEISMIC AND MICROSEISMIC—PART 1

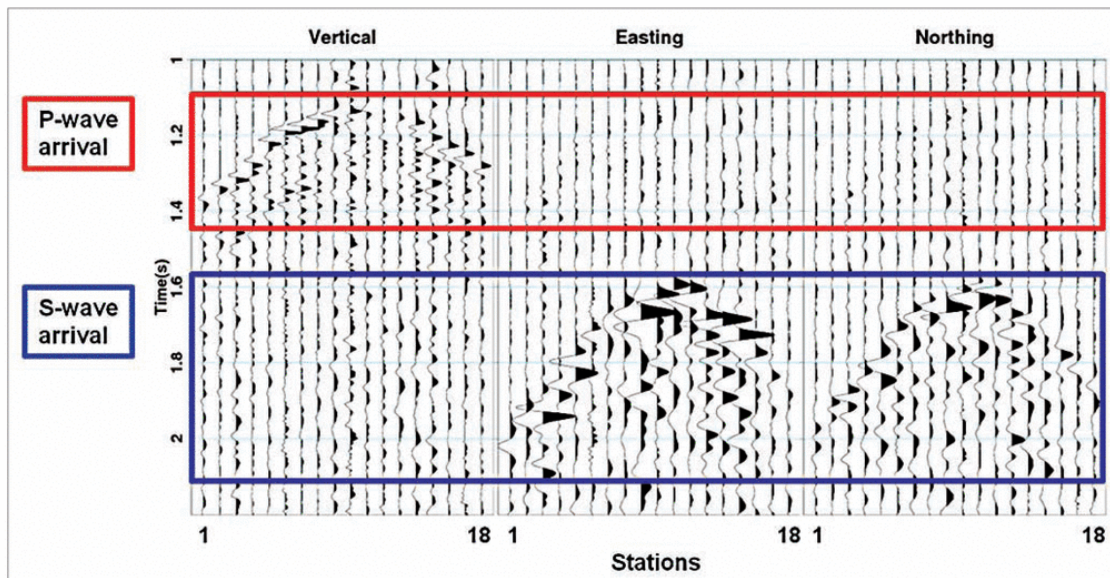


Figure 3. Microseismic arrival on one line of 3C stations perpendicular to the horizontal well. A band-pass filter of 5–90 Hz is applied and relative trace amplitudes are preserved.

vertical and horizontal data components. Microseismic events from depth will have a PS-arrival couplet separated by a narrow range in time as dictated by the reservoir depth and V_p/V_s ratio. This is a powerful QC attribute for eliminating false positives. Events without appropriate PS separation should be discarded. The analysis stage generates three key attributes for each event: the spatial and temporal locations, and the failure mechanism.

Figure 3 shows a characteristic example of a Montney microseismic event from one line of 3C sensors perpendicular to the wells. The P-wave arrival is a clearly visible hyperbola on the vertical component traces with minimum travel time of 1.1 s. The S-wave arrival is most visible on the horizontal traces ~0.5 s later. The amplitude of the S-wave arrival is much stronger and has substantially lower frequency content than the P-wave arrival. We always expect the S-wave energy to have lower frequency content than the P-wave as S-waves travel at lower velocity than P-waves; a shear pulse therefore takes longer to pass a recording sensor and appears lower in frequency.

Figure 4 shows the frequency-time plots with values of power spectral density (PSD) represented by color. Warm colors represent high energy at a given frequency-time pair, while cool colors represent low-seismic energy. The bandwidth for the P-wave arrival in this example ranges from 10 to 90 Hz. The S-wave arrival on the horizontal components has total bandwidth of 5–40 Hz, with the dominant frequency around 12 Hz. In side-by-side comparisons at many locations, we have consistently found that the vertical receiver of a standard, single-component, higher-frequency geophone fails to record all but the strongest S-wave arrivals.

Recording both the P- and S-wave energy allows some flexibility in analyzing event attributes, including event locations. Fracture event locations can be calculated from either P- or S-

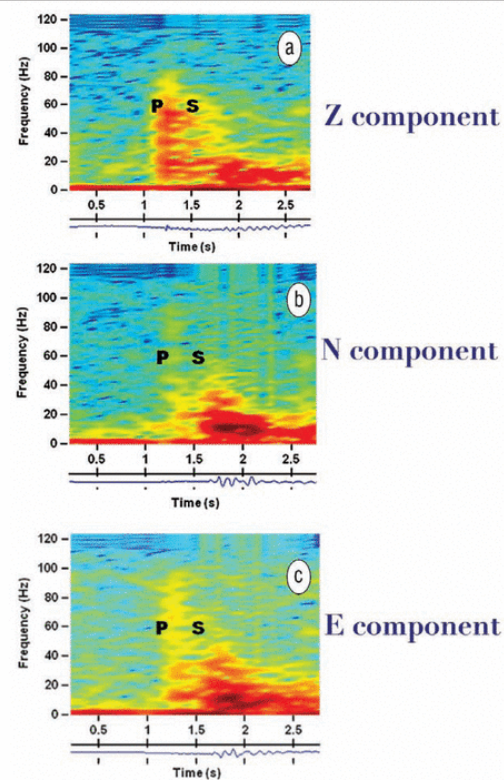


Figure 4. P- and S-wave time-frequency plots of a station from Figure 3.

PASSIVE SEISMIC AND MICROSEISMIC—PART 1

wave arrivals, but the problem is better constrained using both. A useful test is to confirm that both arrivals generate the same location in the subsurface. For this project, perf shots were used to calibrate the velocity model, thereby improving the accuracy of frac event images.

Analysis of the microseismic events used a wave-equation-based depth imaging technique called time-reverse imaging (TRI) (Witten and Artman, 2011). In this technique, recorded, time-reversed trace data are propagated into the velocity model; this process collapses the microseismic hyperboloids back to the location of the frac event. In addition, this technique produces images of the fracture radiation pattern which can be used to interpret fracture source mechanism.

Figure 5 shows an example image from a typical Montney event. Most events in this project share the characteristics of a CLVD fracture type, with a central P-wave focus and two flanking S-wave focus lobes. Panel c shows a constant-amplitude-surface extraction from the volumes in panels a and b. The fracture plane for this event is interpreted to be a plane that passes through the P-wave maximum focus and between the two S-wave lobes. One can see the similarity of this volumetric shape to the surface theoretical radiation pattern maps for the CLVD source shown in Figure 1.

Data analysis. The most valuable analysis step is the interpretation and integration of the processed data with fracture engineering and other geoscience information to generate insights into how a well stimulation program is performing and why. Analysis of microseismic data from these wells began before any event locations were calculated. Event histograms versus time were plotted alongside the frac pumping curves to identify which pumping activities created the events detected in the initial phase of data processing.

Histograms from four stages are shown in Figure 6 to il-

lustrate the variability seen in these data. Individual stages had between 31 and 1710 detected events per stage. Important differences are noted between stages on what pumping activities were related to the onset of detected events, how long events continued after pumping stopped, and the relative frequency of events versus the concentration of proppant in the frac fluid.

On the left of Figure 6a, stage 1 of the upper well has relatively few microseismic events, which is attributed to a smaller volume of fluid and proppant. Immediately after, stage 2 in the lower well, the majority of the events occurred during the six hours after pumping ended. The first stage in panel b, upper well stage 4, had a large number of events that begin only after proppant pumping began, and an increase in event frequency with sand concentration. The last stage presented, stage 4 from the lower well, had the largest total number of events. These begin immediately upon initiation of pumping the fluid-only pad. In most cases, these behaviors largely reflect the presence or absence of pre-existing fractures, which played a large role in the behavior of the frac stages pumped during this project, based on the strong, linear microseismic event location patterns generated by these stages.

Locations calculated for the Montney fractures are shown in Figure 7, segregated by the Upper and Lower Montney zones that produced the events. The events are color-coded by stage with event colors matching the perf zones open during the stage. Note that the Upper Montney frac events tend to be somewhat uniformly distributed in the areas adjacent to the perforations. In contrast, the Lower Montney fracs were heavily influenced by a set of north-south fractures that were activated by all but the first Lower Montney frac stage. The fractures influencing the Lower Montney fracs in this project are attributed to fractures in the underlying Belloy Formation, which influence the Lower Montney but not the Upper Montney

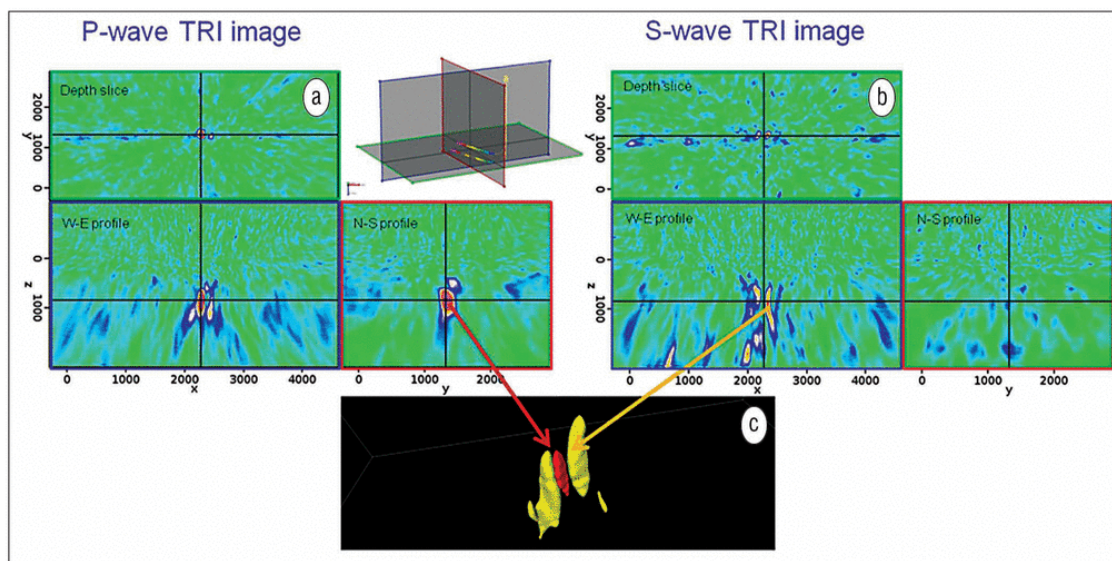


Figure 5. Slices through the (a) P- and (b) S-wave TRI image volumes showing the collapsed radiation of energy from a CLVD fracture. Grey inset with colored borders diagrams the slices extracted in the image panels.

PASSIVE SEISMIC AND MICROSEISMIC—PART 1

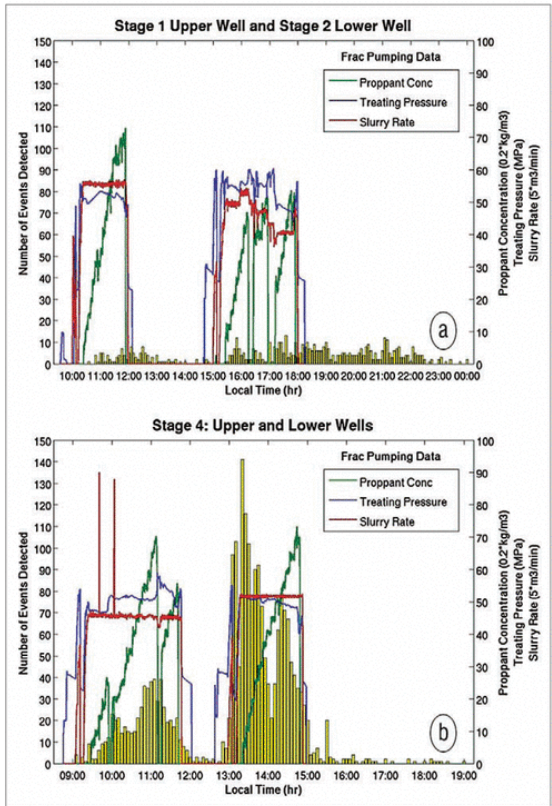


Figure 6. Event histograms showing marked contrasts in fracture development across the completion zones.

treatments. These fractures are visible in 3D seismic data and have been documented in other areas by similar microseismic behavior. More than 30% of the frac events mapped from the Lower Montney well occur below the base of the target zone.

Figure 8 plots the radial distance from the perforation location to the event location versus time and overlays the frac pumping curves for reference. These r-t plots, used by Shapiro et al. (2002), segregate the microseismic events into two populations related to amplitude. In Figure 8a, events are colored by the signal-to-noise ratio. In both stages, a population of stronger events develops close to the well, and is interpreted as fracturing because of the fluid and proppant pumped in the reservoir near the well. A second population of weaker events, further from the well, is attributed to stress effects in the formation ahead of the pumped fluid. These characteristics can be used to discriminate the regions along the lateral which are more likely to be filled with proppant.

In Figure 8b, we discriminate four populations of events based on their location in the r-t space: (1) events created outside of pumping times (red), (2) events created during the pumping of fluid without proppant (green), (3) events created in the near-well environment during proppant pumping (orange), and (4) events created during proppant pumping far away from the well bore (blue).

Microseismic event locations can be converted to an estimate of the stimulated reservoir volume (eSRV) by the fracture treatment in a number of different ways. In this project, we used only the events that could reasonably be expected to be propped open at the completion of the fracture treatment (i.e., the green and orange population in Figure 8b).

In Figure 9, these two event classes are mapped into a 3D reservoir grid. The volume of the grid cells that contained one or more event locations were summed into an effective stimulated reservoir volume. An interesting—and intuitively satisfying—re-

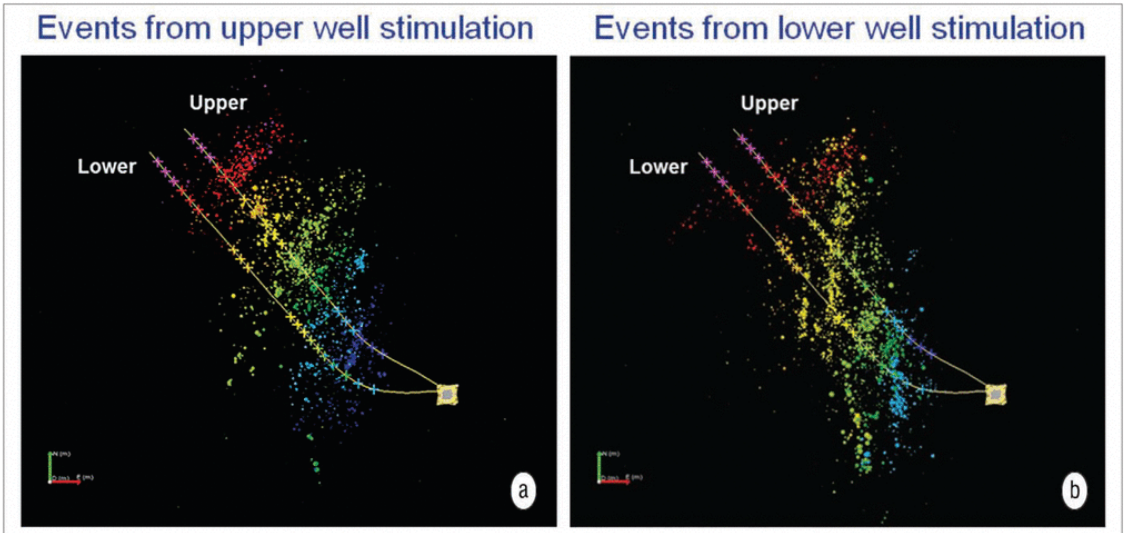


Figure 7. Overhead view of event locations colored by stage (coordinated with colored perforation crosses) for signal-to-noise ratio > 8. (a) Shows events associated with the upper well only, and (b) shows only events from the lower well.

PASSIVE SEISMIC AND MICROSEISMIC—PART 1

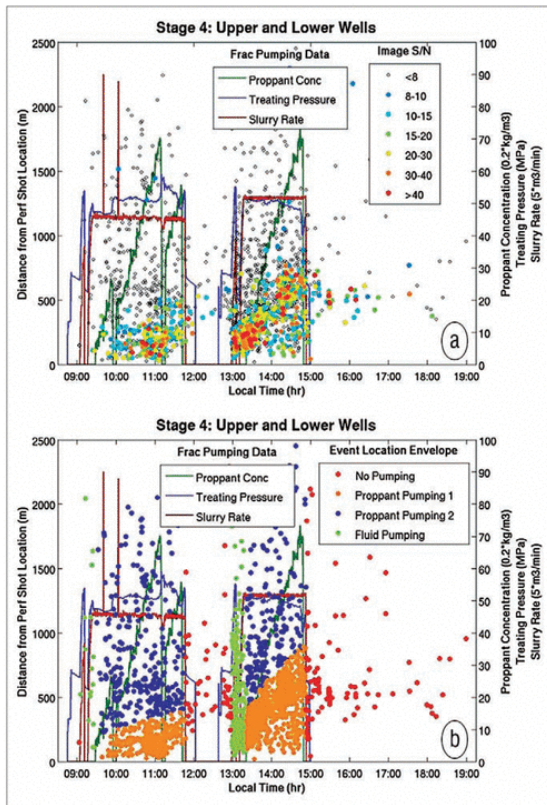


Figure 8. Distance versus time plots for the stages shown in Figure 6b. (a) Events colored by signal-to-noise ratio. (b) Events segregated into populations associated with interpreted fracture mechanisms and stimulation parameters.

sult of this mapping is that the volume of the stimulated reservoir generally scaled linearly with the volume of fluid pumped (Figure 10). Deviations from this trend indicate stages where either the rock took the fracture treatment with reduced pumping effort or stages where the rock was more difficult to stimulate.

Data quality drivers

Local, site-specific parameters contributing to the quality of this data set include the elastic properties of the target interval, which define the seismic efficiency of this suite of rocks to convert the elastic failure of the rock into seismic-wave energy, and the travel path from the source location to the receivers. We have found that areas with high-quality reflection seismic data are similarly amenable to high-quality surface microseismic records; microseismic energy propagates along the same pathways as energy from reflection seismic sources.

Near-surface difficulties, such as peat, swamps, attenuation, and scattering, will affect both types of surveys in the same manner, and incomplete or inappropriate acquisition geometries and instrumentation can fail to record the pertinent information. In addition and in contrast to surface seismic data, a large set of stimulation parameters can influ-

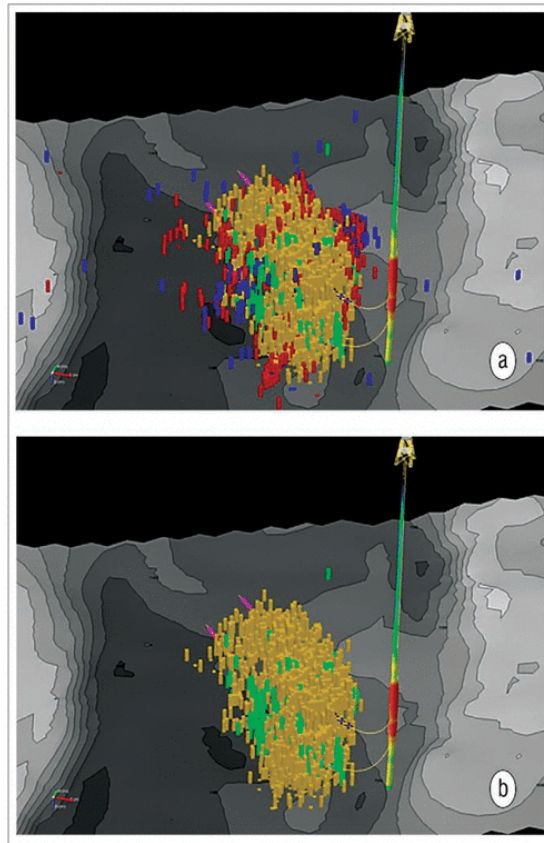


Figure 9. 3D grid mapping of microseismic events with signal-to-noise ratio > 8 colored by event attribute populations as defined in Figure 8b, for all events (a) and the green and orange events (b).

ence microseismic measurements: pump pressure and rate, proppant concentration, fluid and proppant volumes, stage pump time, azimuth of well, and completion style all have an impact on the microseismicity generated.

Conclusions

The microseismic results from these two wells showed that pre-existing fracture trends were an important control on the behavior of the fracture stimulation in this program. Where the pre-existing fractures did not exist, primarily in the upper Montney, frac events typically were recorded only after proppant pumping began and the number of events appears to correlate with proppant concentration. Stimulation of the pre-existing fracture trends in or below the Lower Montney layer resulted in microseismic events that began as soon as frac fluid was pumped into the formation. As many as a third of the frac events from the Lower Montney stimulation occurred in the underlying Belloy Formation.

Mapping fracture events into a 3D geologic grid provides reasonable estimates of stimulated reservoir that can be tied to attributes of the frac stage treatment. These estimates will be integrated with production data to provide better estimates of

PASSIVE SEISMIC AND MICROSEISMIC—PART 1

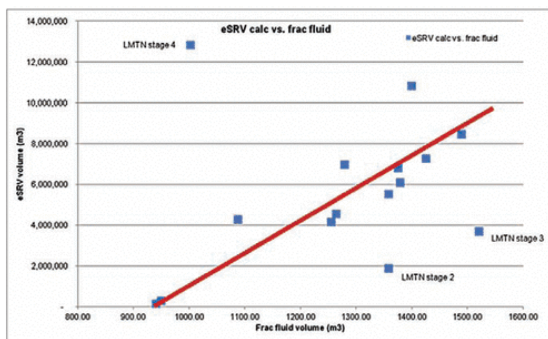


Figure 10. Stage-by-stage crossplot of the stimulated reservoir volume calculated from Figure 9b versus the frac fluid pumped. The red line illustrates the general trend of the data. Outliers to the trend come from the Lower Montney stages.

efficient well and stage spacing, frac design, and well reserve estimates. Fracture trends from the microseismic data can be integrated with 3D seismic attributes to help predict reservoir areas potentially prone to pre-existing fracturing in future development areas, so that these areas can be mapped and developed accordingly.

Seismic emission from fracturing rocks is dominated by S-wave energy. Theory predicts an order of magnitude more shear energy will be emitted from a fracture, and this is borne out by both borehole surveys and our surface data. The results of this project are consistent with our broader database of microseismic surveys, in that the shear waves consistently reach the surface as the strongest part of the fracture wavefield. Where this is contrary to the experience of previous reports, it may be a result of the use of common reflection seismic recording equipment and processing paradigms.

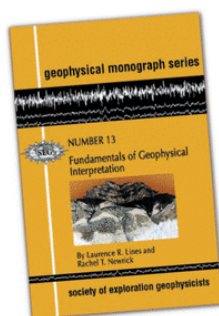
Unconventional reservoirs are a large development target

requiring enormous amounts of capital. Well spacing and stage spacing as well as fracture height in thick reservoirs are probably the primary cost drivers in these developments. Both issues can be addressed, in part, with high-quality microseismic data and analysis. Large fracture systems, as seen in this Montney program, can provide either a robust plumbing system for production or a path for water, depending upon local conditions. Mapping and integration of these fracture systems with other subsurface data such as 3D seismic attributes allows operators to alter their drilling programs to either make use of or avoid these features with future wells. Finally, robust measurements of the volume of the reservoir that is contributing to a well's production are important to production simulation modeling and reserve calculations. **TLE**

References

- Baig, A. and T. Urbanic, 2010, Microseismic moment tensors: A path to understanding frac growth: *The Leading Edge*, **29**, no. 3, 320–324, <http://dx.doi.org/10.1190/1.3353729>.
- Lokmer, I. and C. J. Bean, 2010, Properties from the near-field term and its effect on polarization analysis and source location for long-period (LP) and very-long-period (VLP) seismic events at volcanoes: *Journal of Volcanology and Geothermal Research*, **192**, no. 1–2, 35–47, <http://dx.doi.org/10.1016/j.jvolgeores.2010.02.008>.
- Shapiro, S., E. Rothert, V. Rath, and J. Rindschwentner, 2002, Characterization of fluid transport properties of reservoirs using induced microseismicity: *Geophysics*, **67**, 212–220.
- Witten, B., S. Montgomery, and B. Artman, 2012, Shear wave arrivals in surface microseismic data: 82nd Annual International Meeting, SEG, Expanded Abstracts, <http://dx.doi.org/10.1190/segam2012-0722.1>.
- Witten, B. and B. Artman, 2011, Signal to noise estimates of time-reverse images: *Geophysics*, **76**, no. 2, B1–B10.

Corresponding author: brad.birkelo@spectraseis.com



Fundamentals of Geophysical Interpretation

Laurence R. Lines and Rachel T. Newrick

Fundamentals of Geophysical Interpretation, SEG Geophysical Monograph Series No. 13, is a practical handbook for the petroleum geophysicist. Fundamental concepts are explained using heuristic descriptions of seismic modeling, deconvolution, depth migration, and tomography. Pitfalls in processing and contouring are described briefly. Applications include petroleum exploration of carbonate reefs, salt intrusions, and overthrust faults. The book includes past, present, and possible future developments in time-lapse seismology, borehole geophysics, multicomponent seismology, and integrated reservoir characterization.

ISBN 978-1-56080-125-2
Catalog #153A

Published 2004, 288 pages, Paper
SEG Members \$29, List \$39, E-book \$39



Society of Exploration Geophysicists
The international society of applied geophysics

Order publications online at: www.seg.org/bookmart or E-mail: books@seg.org